



**HAL**  
open science

## Compositional accuracy in atom probe tomography analyses performed on III-N light emitting diodes

Enrico Di Russo, Nikolay Cherkashin, Maxim Korytov, A. Nikolaev, A. Sakharov, A. Tsatsulnikov, B. Bonef, Ivan Blum, Jonathan Houard, Gérald da Costa, et al.

► **To cite this version:**

Enrico Di Russo, Nikolay Cherkashin, Maxim Korytov, A. Nikolaev, A. Sakharov, et al.. Compositional accuracy in atom probe tomography analyses performed on III-N light emitting diodes. *Journal of Applied Physics*, 2019, 126 (12), pp.124307. 10.1063/1.5113799 . hal-02298940

**HAL Id: hal-02298940**

**<https://hal.science/hal-02298940v1>**

Submitted on 21 Nov 2024


**HAL** is a multi-disciplinary open access archive for the deposit and dissemination of scientific research documents, whether they are published or not. The documents may come from teaching and research institutions in France or abroad, or from public or private research centers.

L'archive ouverte pluridisciplinaire **HAL**, est destinée au dépôt et à la diffusion de documents scientifiques de niveau recherche, publiés ou non, émanant des établissements d'enseignement et de recherche français ou étrangers, des laboratoires publics ou privés.

# Compositional accuracy in atom probe tomography analyses performed on III-N light emitting diodes

Cite as: J. Appl. Phys. **126**, 124307 (2019); <https://doi.org/10.1063/1.5113799>

Submitted: 07 June 2019 . Accepted: 31 August 2019 . Published Online: 26 September 2019

E. Di Russo, N. Cherkashin , M. Korytov, A. E. Nikolaev , A. V. Sakharov , A. F. Tsatsulnikov , B. Bonef , I. Blum, J. Houard , G. Da Costa, D. Blavette, and L. Rigutti 



View Online



Export Citation



CrossMark

## ARTICLES YOU MAY BE INTERESTED IN

[Modeling ballistic phonon transport from a cylindrical electron beam heat source](#)

Journal of Applied Physics **126**, 124306 (2019); <https://doi.org/10.1063/1.5115165>

[Nonreciprocity and thermoelectric performance in a double-dot Aharonov–Bohm interferometer](#)

Journal of Applied Physics **126**, 124305 (2019); <https://doi.org/10.1063/1.5111181>

[Study of TaN and TaN-Ta-TaN thin films as diffusion barriers in CeFe<sub>4</sub>Sb<sub>12</sub> skutterudite](#)

Journal of Applied Physics **126**, 125306 (2019); <https://doi.org/10.1063/1.5105385>

## Lock-in Amplifiers up to 600 MHz

starting at

\$6,210



 Zurich  
Instruments

Watch the Video



# Compositional accuracy in atom probe tomography analyses performed on III-N light emitting diodes

Cite as: J. Appl. Phys. 126, 124307 (2019); doi: 10.1063/1.5113799

Submitted: 7 June 2019 · Accepted: 31 August 2019 ·

Published Online: 26 September 2019



E. Di Russo,<sup>1,a),b)</sup> N. Cherkashin,<sup>2</sup> M. Korytov,<sup>2,c)</sup> A. E. Nikolaev,<sup>3</sup> A. V. Sakharov,<sup>3</sup> A. F. Tsatsulnikov,<sup>3,4</sup> B. Bonaf,<sup>5</sup> I. Blum,<sup>1</sup> J. Houard,<sup>1</sup> G. Da Costa,<sup>1</sup> D. Blavette,<sup>1</sup> and L. Rigutti<sup>1</sup>

## AFFILIATIONS

<sup>1</sup>UNIROUEN, INSA Rouen, CNRS, Groupe de Physique des Matériaux, Normandie Université, 76000 Rouen, France

<sup>2</sup>CEMES-CNRS, 29 rue Jeanne Marvig, Toulouse, France

<sup>3</sup>Ioffe Institute, 194021 St. Petersburg, Russia

<sup>4</sup>Submicron Heterostructures for Microelectronics Research and Engineering Center RAS, 194021 St. Petersburg, Russia

<sup>5</sup>Materials Department, University of California, Santa Barbara, California 93106, USA

<sup>a)</sup>Current address: CEA-LETI, Minatec, 38054 Grenoble, France.

<sup>b)</sup>Author to whom correspondence should be addressed: [enrico.dirusso@cea.fr](mailto:enrico.dirusso@cea.fr)

<sup>c)</sup>Current address: IMEC, Kapeldreef 75, B-3001 Heverlee, Belgium.

## ABSTRACT

Laser-assisted atom probe tomography (APT) and high-resolution dark-field electron holography (HR-DFEH) were performed to investigate the composition of a polar [0001] GaN/Al<sub>x</sub>Ga<sub>1-x</sub>N/In<sub>y</sub>Ga<sub>1-y</sub>N light emitting diode. In particular, the III-site fraction of both Al<sub>x</sub>Ga<sub>1-x</sub>N and In<sub>y</sub>Ga<sub>1-y</sub>N alloys was studied adopting a comparative approach. HR-DFEH allows mapping the projected strain with a subnanometer spatial resolution which is used for the calculation of the two-dimensional alloy composition distribution. APT provides three-dimensional alloys composition distribution with a nanometer spatial resolution. However, here we reveal that important inaccuracies affect local composition measurements. A Ga-poor composition is obtained in high DC-electric field regions. Moreover, such inaccuracies may be locally enhanced where the [0001] pole intersects the surface of the analyzed specimen, leading to a lower fraction of Ga measured. III-site fractions closer to the nominal values were measured at low field conditions. Ga loss is thought to be due to preferential DC field induced evaporation of Ga ions between laser pulses. This is explained in terms of formation of a metallic layer on the tip surface during APT analysis, where weak Ga-Ga bonds are formed, promoting the loss of Ga at high field conditions.

Published under license by AIP Publishing. <https://doi.org/10.1063/1.5113799>

## INTRODUCTION

III-V nitride semiconductors based on GaN/In<sub>y</sub>Ga<sub>1-y</sub>N Quantum Wells (QWs) are widely applied in high-power green and violet-blue Light Emitting Diodes (LEDs).<sup>1-3</sup> This is possible thanks to the In<sub>y</sub>Ga<sub>1-y</sub>N bandgap, which ranges from 3.5 eV (GaN) to 0.7 eV (InN). The typical GaN-based LED structure is composed of the following layers: a buffer layer typically grown on an Al<sub>2</sub>O<sub>3</sub> (sapphire) substrate; an n-doped GaN (Si-doped) layer; a GaN/In<sub>y</sub>Ga<sub>1-y</sub>N superlattice; an active region; an Electron Blocking Layer (EBL) formed by an Al<sub>x</sub>Ga<sub>1-x</sub>N barrier; and a p-doped GaN (Mg-doped) contact layer. The active region is formed by single or multiple GaN/In<sub>y</sub>Ga<sub>1-y</sub>N QWs. Recombination of strongly localized excitons in such In<sub>y</sub>Ga<sub>1-y</sub>N

QWs is responsible for the radiative emission of the LED.<sup>4</sup> The number of In<sub>y</sub>Ga<sub>1-y</sub>N QWs, their thickness, and In III-site fraction  $y$  define the LED optical properties such as the emission energy. In particular, higher emission energies can be obtained reducing the In III-site fraction  $y$  in In<sub>y</sub>Ga<sub>1-y</sub>N, decreasing the potential well depth.<sup>5</sup> Moreover, a reduction of the In<sub>y</sub>Ga<sub>1-y</sub>N QW thickness enhances quantum confinement phenomena, increasing the LED emission energy.<sup>6</sup> This effect is particularly enhanced with an increase of the In III-site fraction  $y$  in the QWs.<sup>5,7</sup> Finally, the EBL layer is introduced to prevent carrier leakage into the p-doped GaN layer without compromising the hole injection into the active region. Tuning the Al III-site fraction  $x$  in the Al<sub>x</sub>Ga<sub>1-x</sub>N EBL, the LED optical performances can be significantly improved.<sup>8,9</sup>

The development of GaN-based LEDs clearly requires the careful evaluation of both thicknesses and compositions of  $\text{Al}_x\text{Ga}_{1-x}\text{N}$  and  $\text{In}_y\text{Ga}_{1-y}\text{N}$  layers. Transmission Electron Microscopy (TEM)-based techniques can provide artifact-free atomic-scale images and allow to study strain state, composition, morphology, and growth quality of such heterostructures. However,  $\text{In}_y\text{Ga}_{1-y}\text{N}$  QWs are extremely sensitive to the irradiation produced by the high energy electron beam (>200 keV) used in TEM. The inhomogeneous composition regions formed under electron beam are very similar to those expected from In-rich nanometric-scale regions, even if such issues can be prevented by adopting specific analysis protocols.<sup>10,11</sup>

An alternative and complementary approach is based on Laser-assisted Atom Probe Tomography (La-APT), which provides near atomic-scale three-dimensional (3D) chemical maps. Such an approach has been currently adopted by several authors to study GaN/ $\text{In}_y\text{Ga}_{1-y}\text{N}$  multi-QW systems.<sup>12–24</sup> Nevertheless, atom probe compositional analysis of semiconductors is strongly affected by important biases.<sup>25,26</sup> Recent studies have proved that the measured composition by La-APT principally depends on the intensity of the standing field (DC field) applied on the APT specimen.<sup>26–29</sup> In addition, the specimen crystallography affects the DC field distribution on the tip surface, in particular for specimens analyzed along the [0001] direction. As a consequence, position-dependent composition biases can be observed over the analyzed surface.<sup>27,29</sup>

The present work is focused on the III-site fraction quantification in  $\text{Al}_x\text{Ga}_{1-x}\text{N}$  and  $\text{In}_y\text{Ga}_{1-y}\text{N}$  layers grown in a *c*-axis oriented (wurtzite crystal) LED structure. Several investigations have already addressed the problem of composition in  $\text{Al}_x\text{Ga}_{1-x}\text{N}$  alloys. However, no systematic study has been conducted in polar  $\text{In}_y\text{Ga}_{1-y}\text{N}$  alloys.<sup>26,30–32</sup> The main advantage of studying the III-site fraction is that measurements are independent of the amount of nitrogen detected. Nitrogen quantification artifacts reproduce what has been previously reported<sup>25,26</sup> and are not considered in this article. The production of neutral N (i.e., following dissociation processes) is in fact proposed as the loss mechanism explaining the N-poor composition observed at low field in III-N semiconductors.<sup>27,33,34</sup> Therefore, a systematic investigation of III-site fractions may elucidate the physical mechanisms responsible for the loss of specific metallic atoms during atom probe analyses.

The interest of the present study is twofold. On the one hand, it provides operational guidelines for an accurate composition analysis of LED structures by APT. On the other hand, the experimental results represent a significant gain in the understanding of microscopic field evaporation mechanisms in these materials.

## MATERIALS AND METHODS

The sample investigated is a GaN/ $\text{Al}_x\text{Ga}_{1-x}\text{N}$ / $\text{In}_y\text{Ga}_{1-y}\text{N}$  LED emitting at about 540 nm (yellow-green). The heterostructure was grown on (0001) sapphire substrate by Metal Organic Vapor Phase Epitaxy (MOVPE) in an AIX2000HT 6×2 in. planetary reactor. The structure consists of ~5 μm GaN buffer layer, 24 nm (6 nm— $\text{In}_y\text{Ga}_{1-y}\text{N}$ /2 nm—GaN) superlattice (SL), and 15 nm n-GaN barrier grown at 915 °C, 3 nm  $\text{In}_y\text{Ga}_{1-y}\text{N}$  QW grown at 825 °C, 4 nm undoped GaN barrier grown at 900 °C, 11 nm p- $\text{Al}_x\text{Ga}_{1-x}\text{N}$  EBL, and 120 nm p-GaN grown at 1000 °C. The SL was formed using the growth interruption approach.<sup>35</sup>

A Scanning Electron Microscope/Focused Ion Beam (SEM/FIB) was used to prepare a TEM lamella and needle-shaped tips required for La-APT. The specimen preparation method consisted in a standard lift out procedure followed by milling with 30 kV Ga ions and cleanup procedure at 2 kV in order to reduce the thickness of the damaged volume.<sup>36–38</sup>

TEM investigations were carried out using I2TEM–Toulouse, a HF3300 (Hitachi) TEM operating at 300 kV, equipped with a cold-field emission source, an imaging aberration corrector (CEOS B-COR), a multiple biprism system, and a 4k CCD camera. High-Resolution Dark-Field Electron Holography (HR-DFEH) experiments were performed with the sample holder position within the objective lens. Contrary to the Lorentz-DFEH,<sup>39–41</sup> such mode does not allow large (~1 μm) field of view. However, thanks to a 0.1 nm fringe spacing and image aberration correction, HR-DFEH provides ultimate spatial resolution of at best 0.3 nm for strain mapping which is essential for the analysis of extremely thin layers.<sup>42</sup> The holograms were recorded using ⟨0008⟩ diffracted beam. Out-of-plane strain maps were reconstructed using HoloDark plugin for DigitalMicrograph.<sup>43</sup> Out-of-plane strain distribution maps were obtained over 70 × 70 nm fields of view with a 0.6 nm spatial resolution and 0.1% precision. In order to correct the measured strain values for the impact of stress relaxation at the free surfaces of the TEM lamellas, we have applied the Finite Element Method (FEM) modeling within COMSOL Multiphysics software. Indium and aluminum composition maps were extracted from the corrected out-of-plane strain maps by using elasticity theory for biaxially stressed pseudomorphic to the substrate 2D layers.<sup>44–46</sup> Finally, the method allowed the extraction of composition maps in the  $\text{Al}_x\text{Ga}_{1-x}\text{N}$  and  $\text{In}_y\text{Ga}_{1-y}\text{N}$  layers with an accuracy of at most 2% in *x* and *y*.

Atom probe analysis was performed using a FlexTAP (CAMECA) tomographic atom probe operated with femto-second laser pulses (350 fs) at a wavelength of  $\lambda = 343$  nm (UV). The pulses repetition frequency was 50 kHz. The laser pulse energy  $E_{las}$  was 1.0 nJ, corresponding to a peak energy density during the pulse of  $\sim 10^{-4}$  J cm<sup>2</sup>. The field of view was fixed at ±15°. The specimen was cooled to a base temperature of 80 K. La-APT analyses were performed at a constant detection rate ( $\varphi \approx 0.0025$  event/pulse), varying the applied bias  $V_{DC}$  in order to keep  $\varphi$  constant during the tip evaporation. The detection system used was a specially designed Multi-Channel Plate/advanced Delay Line Detector (MCP/aDLD) with a MCP detection efficiency  $\eta_{MCP}$  of  $\approx 0.6$ .<sup>46,47</sup> It should be noted that the analysis conditions are very similar to those used for GaN in a previous work.<sup>26</sup>

## RESULTS AND DISCUSSION

### Electron microscopy

A HR-DFEH out-of-plane strain map of the LED heterostructure is represented in Fig. 1(a). The material deformation is measured with respect to the zero strained GaN lattice. The large lattice mismatch between GaN and  $\text{In}_y\text{Ga}_{1-y}\text{N}$  alloys is responsible for the tensile out-of-plane strain observed in  $\text{In}_y\text{Ga}_{1-y}\text{N}$  pseudomorphic to the substrate layers. More In incorporated into these layers results in higher measured strain. Similarly, compressive out-of-plane strain is observed in the  $\text{Al}_x\text{Ga}_{1-x}\text{N}$  alloy which has lower lattice

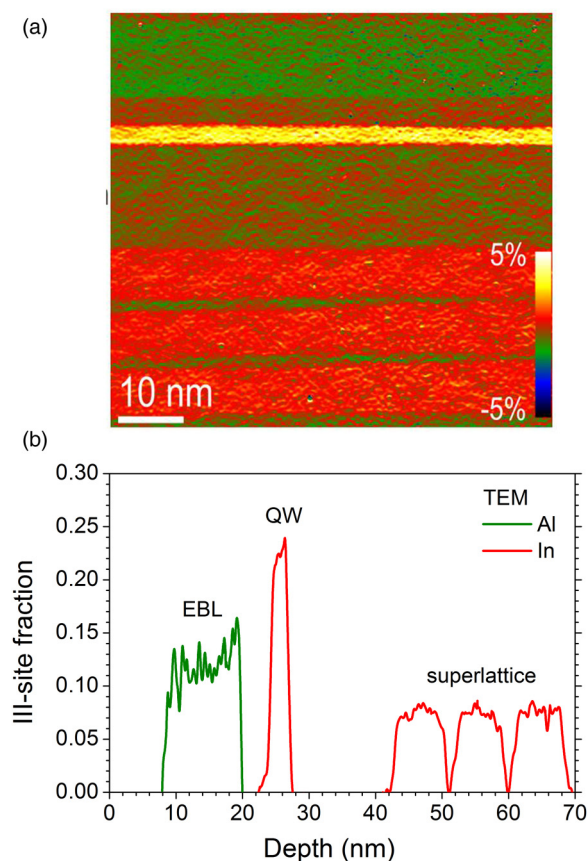


**FIG. 1.** (a) HR-DFEH strain map of a lamella specimen. (b) Al and In III-site fraction profiles along the c-axis direction derived from the strain map.

parameters than GaN matrix. Again, the effect strictly depends on the Al content. Once the measured strain values were corrected by a factor of 1.16 for the effect of stress relaxation in a TEM lamella, the composition within the alloys was extracted from the elasticity theory.<sup>44–46</sup> In this way, the III-site fraction associated to both  $\text{Al}_x\text{Ga}_{1-x}\text{N}$  and  $\text{In}_y\text{Ga}_{1-y}\text{N}$  alloys can be assessed with an accuracy of  $\sim 0.02$ . The composition profiles calculated along the c-axis direction of the LED are reported in Fig. 1(b). The three  $\text{In}_y\text{Ga}_{1-y}\text{N}$  layers composing the superlattice exhibit an In content equal to 0.08, while the measured In fraction in the active QW reaches 0.24. This In fraction is in agreement with the values expected to generate green light in c-plane LED.<sup>49</sup> Lastly, the Al III-site fraction associated to the  $\text{Al}_x\text{Ga}_{1-x}\text{N}$  EBL is about 0.15.

### Mass spectra

The mass spectrum related to the atom probe analysis of the specimen is represented in Fig. 2(a). A total number of  $1.5 \times 10^6$  events were detected. The choice for the mass spectrum peak indexing is the same reported in the literature.<sup>18,25,27,29,34</sup> Nitrogen

is predominantly evaporated as  $\text{N}_2^+$  ions and forms a peak at 28 Da. Also, a few  $\text{N}_3^+$  ions are detected at 42 Da. The peak at 14 Da is associated to  $\text{N}^+$  ions.  $\text{Ga}^+$  ions are associated with the peaks observed at 69 and 71 Da, because of its two isotopes. The peaks at 34.5 and 35.5 Da are due to the presence of  $\text{Ga}^{2+}$  ions. Some heterogeneous molecular ions are recognized. These are as follows:  $\text{GaN}^{2+}$ , forming a pair of peaks at 41.5 and 42.5 Da;  $\text{GaN}_3^{2+}$ , observed at 55.5 and 56.5 Da. The mass spectrum of the EBL is represented in Fig. 2(b). About  $1 \times 10^5$  events are recorded. Three different peaks associated to  $\text{Al}^+$ ,  $\text{Al}^{2+}$ , and  $\text{Al}^{3+}$  ions appear at 27, 13.5, and 9 Da, respectively. Also few  $\text{AlN}^{2+}$  ions are detected at 20.5 Da. Lastly, in Fig. 2(c), the mass spectrum of the  $\text{In}_y\text{Ga}_{1-y}\text{N}$  layer #1 is reported [cf. Fig. 3(a)]. A total number of  $8 \times 10^4$  events are associated to this layer. It presents two isotopes with mass numbers 113 and 115. The first has a natural abundance of about 4% while the second one of about 96%. Moreover,  $\text{In}^{2+}$  ions are detected at 56.5 and 57.5 Da. It should be observed that the minor peak of  $\text{In}^{2+}$  ions is perfectly superimposed with the  $\text{GaN}_3^{2+}$  peak present at 56.5 Da. In order to carefully determine the composition a peak decomposition procedure must be carried out. Briefly, the number of  $\text{In}^{2+}$  ions present at 56.5 Da was calculated knowing that 95.7% of  $\text{In}^{2+}$  ions forms the peak at 57.5 Da. The number of  $^{113}\text{In}^{2+}$  ions at 56.5 Da can then be straightforwardly determined. The rest of the events at 56.5 Da is attributed to  $\text{GaN}_3^{2+}$ . Parasitic species (such as hydrogen-, carbon-, nitrogen-, and oxygen-related peaks) and hydrides were also detected, most likely supplied by the environment during the specimen preparation procedure and during La-APT analysis.

### Atom probe 3D reconstruction

The 3D reconstructed volume of the tip analyzed is represented in Fig. 3(a).  $\text{Al}^+$ ,  $\text{Al}^{2+}$ , and  $\text{Al}^{3+}$  ions are represented in green and  $\text{Ga}^+$  and  $\text{Ga}^{2+}$  in blue.  $\text{In}^+$  and  $\text{In}^{2+}$  ions are depicted in red. A cone-angle reconstruction algorithm is applied using the tip geometrical features observed using SEM. The reconstruction parameters are as follows: apex radius: 35 nm; tip cone angle: 15°; curvature: 1; and reconstruction efficiency: 0.20. The latter parameter was chosen in order to scale the depth direction of the APT reconstruction with the layer thicknesses provided by TEM images. The other parameters are fitted in order to obtain a reconstructed volume with flat layers in agreement with the thicknesses measured by high-resolution TEM. The III-site fraction profile extracted along the c-axis direction of the atom probe 3D reconstruction is reported in Fig. 3(b). It is very interesting to compare this profile with the one derived from the strain map in Fig. 1(b). The results obtained from the two different techniques present remarkable differences. First, both Al and In III-site fractions measured with atom probe are greater than the respective fractions provided studying the strain state by HR-DFEH. Second, the spatial resolution provided by La-APT ( $\sim 2$  nm) is lower compared to the one reached performing HR-DFEH ( $\sim 0.6$  nm).

### Considerations about charge-state metrics

As demonstrated in previous works, the Charge-State Ratio (Ga-CSR) allows the electric field to be assessed.<sup>25–30,34</sup> The so-called effective field  $F_{\text{eff}}$  can be estimated by the ratios of

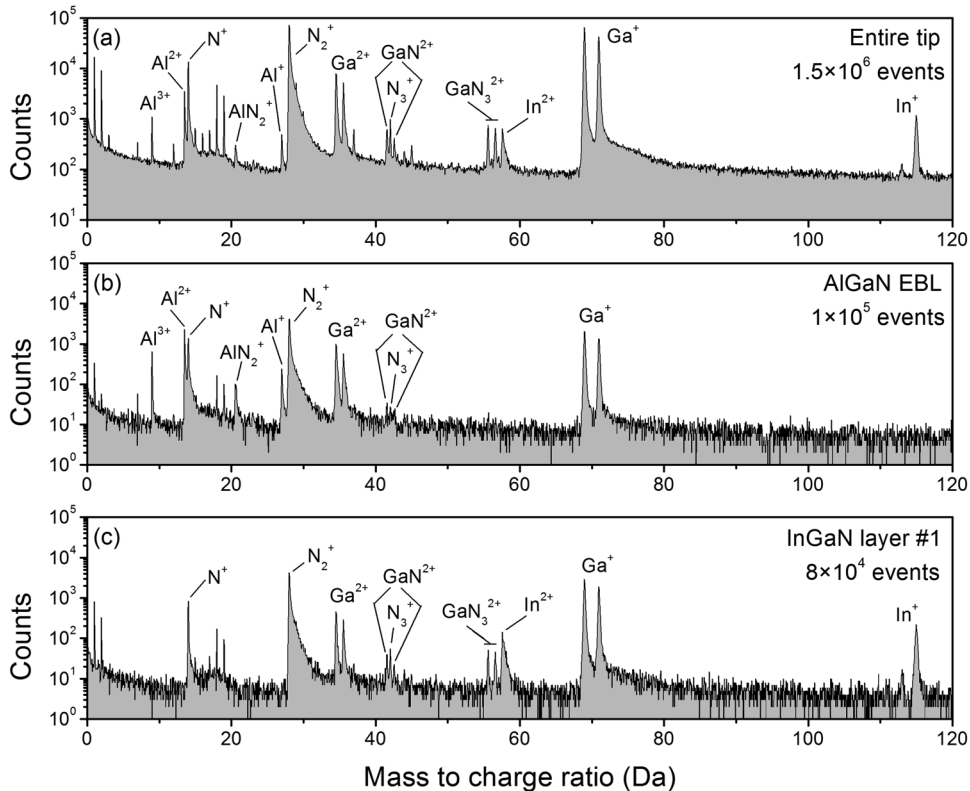


**FIG. 2.** Mass spectra of the LED atom probe specimen associated to (a) the entire volume analyzed; (b) the  $\text{Al}_{0.15}\text{Ga}_{0.85}\text{N}$  EBL; and (c) the  $\text{In}_{0.08}\text{Ga}_{0.92}\text{N}$  layer #1 [cf. Fig. 3(a)]. Tomographic atom probe used: FlexTAP. UV laser pulse energy:  $E_{\text{las}} = 1$  nJ. Tip base temperature:  $T = 80$  K. Field of view:  $\pm 15^\circ$ . Detection rate:  $\varphi \approx 0.0025$  event/pulse.

different charge states of given species through Kingham's postionization model.<sup>50</sup> Briefly, the intense electric field is responsible of the evaporation of single charged ions from the tip surface. However, postionization can occur close to the tip surface. When an ion reaches a critical distance from the tip surface (several angstroms), additional electrons can be transferred from the ion to the tip surface by quantum tunneling effects. In principle, the process is not influenced by the specimen. Moreover, the calculation of  $F_{\text{eff}}$  can be done with any species, even if most of the time only metallic elements are considered. In the case of the  $\text{Al}_{0.15}\text{Ga}_{0.85}\text{N}$  EBL, both Ga-CSR ( $\text{Ga}^{2+}/\text{Ga}^+$ ) and Al-CSR ( $\text{Al}^{2+}/\text{Al}^+$ ) were considered. In particular, the EBL was divided into subregions along the  $c$ -axis direction adopting the approach detailed in Refs. 25 and 30. For each subregion, both Ga-CSR and Al-CSR are calculated. The relation between the two ratios is represented in Fig. 4(a), where also the  $F_{\text{eff}}$  provided by the postionization theory is reported. The data reveal that the field estimated by the Al-CSR metric (from 24 to 25 V/nm) is lower compared to the one derived using the Ga-CSR metric (from 25 to 27 V/nm). However, the estimate of  $F_{\text{eff}}$  by an Al-CSR is questionable. In fact,  $\text{Al}^+$  and  $\text{Al}^{3+}$  ions are not expected to be observed at the same time by the postionization theory.<sup>26,30</sup>  $\text{Al}^+$  ions should be completely postionized forming  $\text{Al}^{2+}$  ions at about 26 V/nm, while  $\text{Al}^{3+}$  ions should be observed starting from about 38 V/nm.<sup>50</sup> For this reason, in  $\text{Al}_y\text{Ga}_{1-y}\text{N}$  alloys the  $F_{\text{eff}}$  is generally estimated considering only the Ga-CSR. The simultaneous presence of different charge-state ratios of Al ions can reflect

the variations of field at the tip surface at the atomic scale (atomic protuberances, neighborhood of the emitted ion, etc.). In the InGaN layers of the SL, both In-CSR ( $\text{In}^{2+}/\text{In}^+$ ) and Ga-CSR were calculated. The relation between these quantities is depicted in Fig. 4(b). Again, the effective fields derived from both In and Ga are not consistent. The field estimated by In-CSR (from 21 to 23 V/nm) is lower than the field calculated by Ga-CSR (from 23 to 25 V/nm). This suggests again that the postionization theory cannot be strictly applied to calculate the electric field, as already suggested.<sup>28,30</sup> Therefore, Ga-CSR can be reliably used to estimate the variations of the effective field  $F_{\text{eff}}$  in all analyzed parts of the specimen. Such ratio is thus recommended to be adopted to describe the field-dependence of composition in both  $\text{Al}_x\text{Ga}_{1-x}\text{N}$  and  $\text{In}_y\text{Ga}_{1-y}\text{N}$  alloys.

### Composition analysis

The local, nanometer-scale composition distribution in  $\text{Al}_{0.15}\text{Ga}_{0.85}\text{N}$  EBL was investigated. For that purpose, the EBL was divided into about 200 subregions, adopting the method described in Ref. 30. For each subregion, both Ga-CSR and Al III-site fraction  $x$  were measured. The Ga-CSR map obtained from the EBL analysis is represented in Fig. 5(a). The image exhibits a radial symmetry around a high field region, associated with the presence of the [0001]-pole. This field distribution is a direct consequence of the tip faceting due to the crystallography:

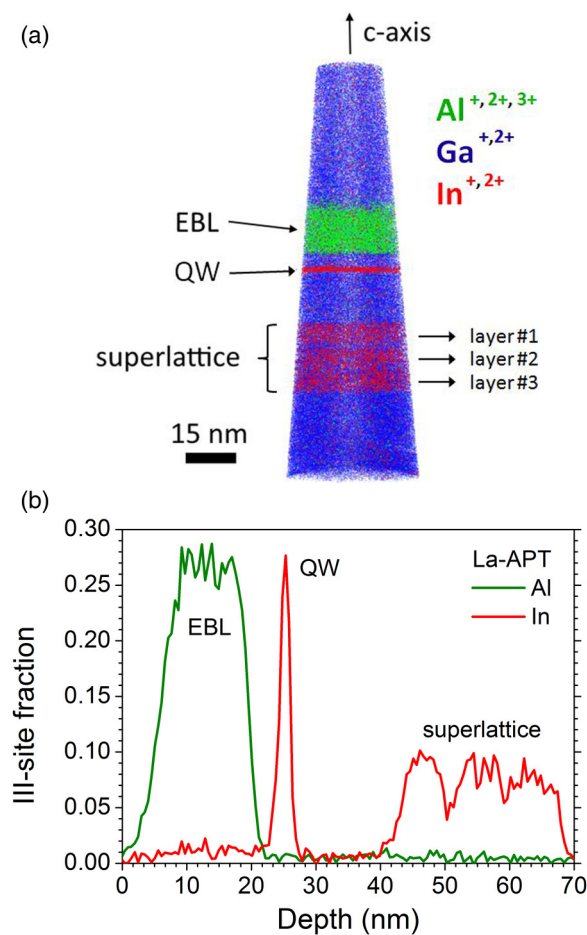


**FIG. 3.** (a) 3D reconstruction of the LED volume analyzed using FlexTAP. The reconstruction was performed using the cone-angle algorithm with the following parameters: apex radius: 35 nm; tip cone angle: 15°; curvature: 1; reconstruction efficiency: 0.20. (b) Al and In III-site fraction profiles along the c-axis direction measured using atom probe.

low index poles (i.e., [0001]-pole) present a lower radius of curvature compared to high index poles. This leads to local variation of the field (averaged over time) over the tip surface. The Al III-site fraction map is reported in Fig. 5(b). Comparing the two maps, it is clear that high field regions are associated with higher Al III-site fractions measured. In order to point out such relation, the probed tip surface was divided into about 40 subregions and the Al III-site fraction is plotted as a function of the Ga-CSR for each of them in Fig. 5(c). The Ga-CSR distribution reveals that  $F_{\text{eff}}$  ranges between 25 and 27 V/nm. At low field conditions,  $x \approx 0.2$  ( $F_{\text{eff}} \approx 25$  V/nm). As the effective field increases,  $x$  is increased up to 0.35 ( $F_{\text{eff}} \approx 27$  V/nm). Nevertheless, the nominal Al III-site fraction ( $x = 0.15$ ) was never measured within the electric field conditions investigated. More details of the Al III-site fraction dependence on the experimental condition for alloys with

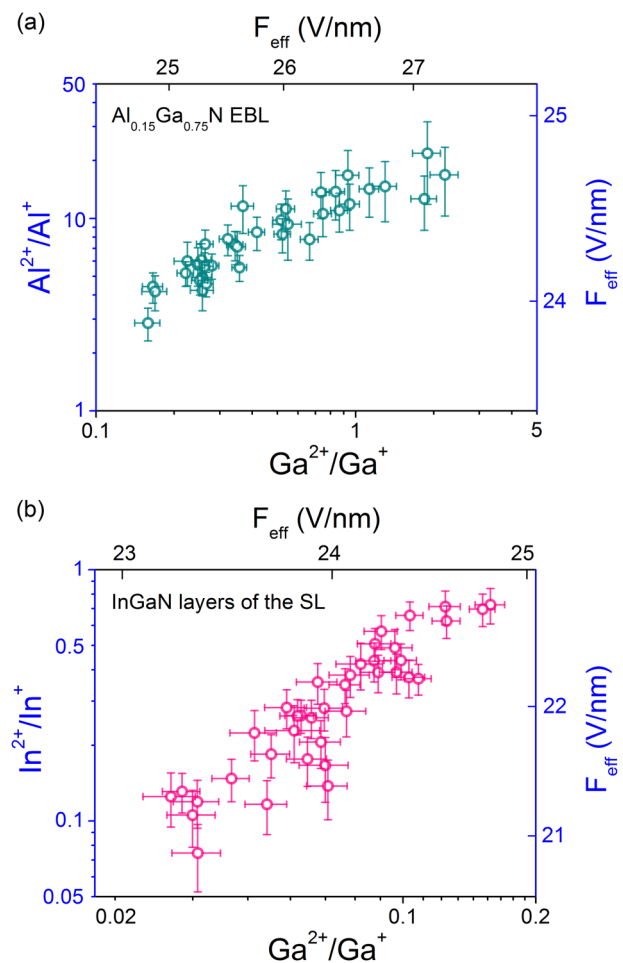


**FIG. 4.** (a) Comparison between the experimental Ga- and Al-CSR observed in  $\text{Al}_{0.15}\text{Ga}_{0.85}\text{N}$  EBL. (b) Relation between the experimental Ga- and In-CSR observed in the InGaN layers of the SL. The values of  $F_{\text{eff}}$  are calculated according to the positionization model.

different Al content can be found in previous studies.<sup>26,30,31</sup> In order to explain these results, the Ga atoms loss mechanism between laser pulses was recently proposed.<sup>26,30</sup> As a consequence of such Ga loss channel, a higher Al III-site fraction  $x$  is obtained. This explains why the measured Al III-site fraction increases with the applied field.

The approach adopted for the EBL was extended to the  $\text{In}_y\text{Ga}_{1-y}\text{N}$  layers. First of all, the local distribution of both Ga-CSR and In III-site fraction in the  $\text{In}_{0.24}\text{Ga}_{0.76}\text{N}$  QW was investigated. Results are depicted in Fig. 6. The correlation between the surface field [Fig. 6(a)] and the composition [Fig. 6(b)] is similar to the one observed for the EBL. The high field region in correspondence of the [0001]-pole is associated with an In III-site fraction up to about 0.35. Instead, low field regions present a composition close to the value derived by the strain state map (0.24).

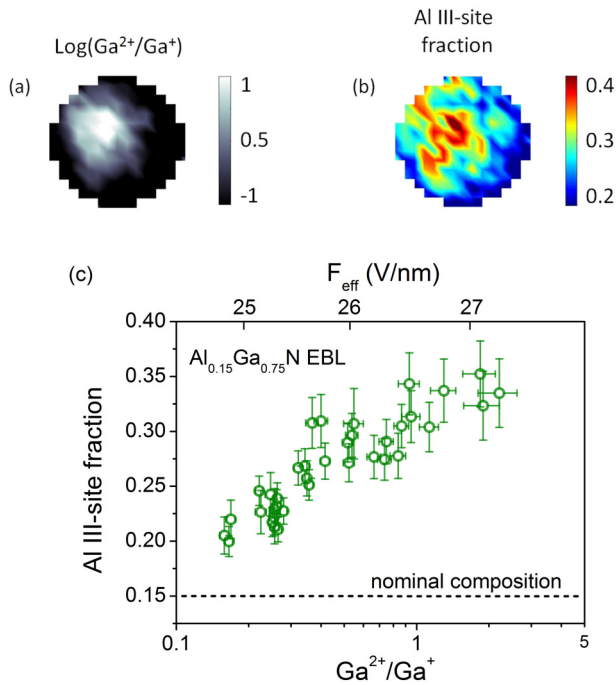


**FIG. 5.** (a) Ga-CSR and (b) Al III-site fraction chart of the  $\text{Al}_{0.15}\text{Ga}_{0.85}\text{N}$  EBL. (c) Al III-site fraction plotted as the function of the local Ga-CSR. The effective field  $F_{\text{eff}}$  is calculated from the Ga-CSR through the postionization theory.

The composition of the three  $\text{In}_{0.08}\text{Ga}_{0.92}\text{N}$  layers forming the superlattice was subsequently investigated. The local distribution of the Ga-CSR is reported in Figs. 7(a)–7(c). Again, a high field region is observed in correspondence with the [0001]-pole.  $F_{\text{eff}}$  is estimated between 21 and 24 V/nm. Moreover, a higher field intensity is observed in layer #1 [Fig. 7(a)]. Ga-CSR (resp.  $F_{\text{eff}}$ ) decreases in layer #2 [Fig. 7(b)] and again in layer #3 [Fig. 7(c)]. This is the consequence of the competition between various effects, such as the increase of the tip radius, the reduction of the magnification, and the increase of the tip surface probed. In fact, at a constant detection rate ( $\phi = \text{const.}$ ), the  $V_{\text{DC}}$  bias applied dynamically changes during the tip evaporation. In a homogeneous specimen, despite the  $V_{\text{DC}}$  bias increases with time, the electric field on the

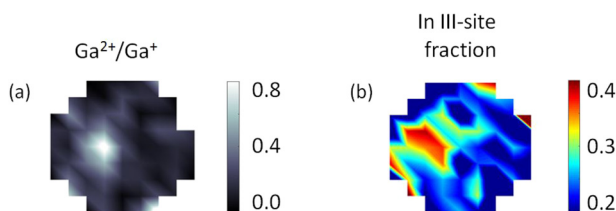


**FIG. 6.** (a) Ga-CSR and (b) In III-site fraction chart of the  $\text{In}_{0.24}\text{Ga}_{0.76}\text{N}$  quantum well.

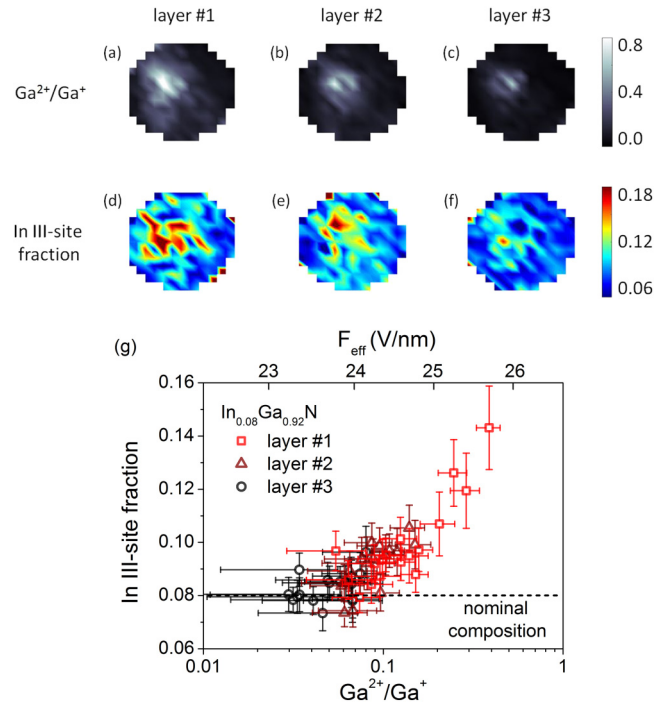


**FIG. 7.** (a)–(c) Ga-CSR and (d)–(f) In III-site fraction chart of the  $\text{In}_{0.08}\text{Ga}_{0.92}\text{N}$  layers. (g) In III-site fraction plotted as the function of the local Ga-CSR. The effective field  $F_{\text{eff}}$  is calculated from the Ga-CSR through the postionization theory.

tip surface decreases because the tip angle increases (shank angle of tip). In the case of a heterostructure, variations of the applied  $V_{\text{DC}}$  bias are observed at the interfaces between materials presenting different evaporation fields. Despite this, an overall reduction of the electric field at the tip surface is always observed during the tip evaporation. Such progressive field reduction during an atom probe analysis is the so-called cone-angle effect.<sup>26</sup> The spatial distribution of In III-site fraction at the tip surface of  $\text{In}_{0.08}\text{Ga}_{0.92}\text{N}$  layers is represented in Figs. 7(d)–7(f). Again, a correlation exists between a local field and the measured composition. The measured In III-site fraction  $y$  is higher at high field regions due to Ga preferential evaporation. Moreover, a progressive diminution of the In III-site fraction is observed corresponding to a progressive decrease of the field [Figs. 7(d)–7(f)]. This effect is highlighted in Fig. 7(g), where the local III-site fraction  $y$  is plotted as a function of the Ga-CSR for the three InGaN layers investigated. The effective field  $F_{\text{eff}}$  is calculated from the Ga-CSR. Data indicate that  $y$  is always overestimated at high field conditions. This is particularly evident in layer #1 where  $y$  ranges from 0.09 to 0.14 for an effective field  $F_{\text{eff}}$  ranging from 23 to 26 V/nm, respectively. Only at low field conditions (from 23 to 24 V/nm), the measured local In III-site fraction tends to the nominal value (0.08) over the whole tip surface, as it is clearly observed in layer #3. An In III-site fraction lower than the nominal one was never observed. This behavior is very similar to that observed in AlGa<sub>x</sub>N, MgZnO, and BGaN alloys.<sup>26,29–31</sup>



The microscopic composition distribution detected for [0001]-oriented InN is reported in the [supplementary material](#).

### Mechanisms leading to compositional biases

The observed dependence of the III-site compositions on the DC field provides important information regarding the complex phenomena leading to the laser-assisted field evaporation process. The analysis of mass spectra of different semiconductors acquired under various experimental conditions strongly suggests that the overall process is the result of the competition between at least three different phenomena. First, short-range atom migration can occur due to laser heating and the presence of electric field gradient over the tip surface, promoting the formation of clusters, in particular, in the presence of group V elements.<sup>25,27,28,51,52</sup> Second, high electric field conditions are responsible for the dissociations of these clusters on the tip surface or during their flight toward the detector.<sup>28,53</sup> The deficit of N at low field is probably related to such a process, i.e., the emission of neutral N upon dissociation of  $\text{GaN}^+$  ions.<sup>25,27</sup> Finally, differences in the binding energy of surface atoms can lead to preferential evaporation of the more weakly bound species (i.e., evaporation uncorrelated to laser pulses, leading to the impossibility of identifying the correct mass to charge ratio by time-of-flight mass spectrometry). In the present case, preferential evaporation of Ga atoms can be identified as the main mechanism responsible for the composition biases observed in both  $\text{Al}_x\text{Ga}_{1-x}\text{N}$  and  $\text{In}_y\text{Ga}_{1-y}\text{N}$  alloys. This should be explained in terms of the differences in the binding energies and, as a consequence, in the evaporation fields ( $F_{ev}$ ) of Ga, Al, and In in the respective alloys. As Ga-depleted composition is observed at high field conditions for both alloys, the  $F_{ev}$  of Ga is necessarily lower than those of both Al and In. The development of a simple model describing preferential evaporation has recently allowed estimating the  $F_{ev}$  of Ga and Al in AlGaN of about 25 and 27 V/nm, respectively.<sup>26</sup> Moreover, the same considerations applied to data reported in Fig. 7(g) provide an estimation of  $F_{ev}$  of about 24 and 26 V/nm for Ga and In in InGaN, respectively. The different evaporation fields of Al, Ga, and In cannot be a direct consequence of their different bulk binding energies, where metallic elements are bound to N atoms only. It is well known that the Al-N cohesive energy ( $E_c = 13.2$  eV) is higher than the Ga-N one ( $E_c = 10.1$  eV), while the In-N bond is the weakest one ( $E_c = 8.7$  eV).<sup>54,55</sup> This is in contrast with the Ga-poor composition observed in  $\text{In}_y\text{Ga}_{1-y}\text{N}$  (Fig. 7). In atoms should be lost in larger quantities at higher fields. Nevertheless, the stability of surface atoms in group III-nitrides and their alloys is affected by surface reconstruction processes. In fact, one or more stable metal-rich layers can be formed at the top surface, presenting weaker metallic bonds.<sup>56</sup> Moreover, heating effects due to the laser pulses during La-APT significantly increase the tip surface temperature promoting diffusion phenomena.<sup>52,57</sup> Short-range diffusion phenomena are dominant as attested by the massive presence of  $\text{N}_2^+$  molecules in III-N mass spectra (Fig. 2), despite no N-N bonds are expected in the crystals.<sup>25,27,30</sup> In the case of metals, adatoms migration strongly increases for low melting point ( $T_{melt}$ ) elements.<sup>52</sup> The high mobility and the very low melting point of Ga adatoms compared to In or Al [ $T_{melt}(\text{Ga}) = 300$  K,  $T_{melt}(\text{In}) = 430$  K,  $T_{melt}(\text{Al}) = 930$  K, under

standard conditions] can lead to the formation of weak Ga-Ga bonds on the tip surface.<sup>58</sup> Other metallic bonds involving In and Al may form, but Ga adatoms are those that can more easily evaporate uncorrelated with laser pulses.<sup>56</sup> This result is in agreement with the model describing the formation of laterally contracted metallic Ga bilayers that can be energetically favorable on GaN surfaces under Ga-rich conditions.<sup>59</sup> In our case, the preferential loss of N by different evaporation channels could be the driving mechanism leading to Ga-rich conditions at the surface.<sup>25–27</sup> Intriguingly, metallic Ga bilayers are known to occur in very different situations, i.e., during the GaN growth by molecular beam epitaxy (MBE): in this case, the Ga-rich conditions are assured by the regulation of the molecular fluxes impinging on the surface.<sup>60</sup> The formation of a Ga (Al, In) metallic layer on a III-N surface under high electric field also represents an alternative picture of the so-called metallization of apices of field-emission dielectric tips during APT analyses with respect to the proposed mechanism of hole accumulation induced by band bending and impact ionization.<sup>61</sup>

### Indications for APT users

In order to measure III-site fractions closer to nominal values, various strategies can be adopted. First of all, the cone-angle effects inducing large variations of electric field during the analysis can be partially mitigated with a specific FIB specimen preparation. A reduction of the specimen cone-angle and an increase of the initial tip radius lead to lower and more constant over time electric field during La-APT. Secondly, the atom probe analysis parameters can be tuned. In particular, an augmentation of the laser pulse energy  $E_{las}$  at a constant detection rate leads to a reduction of the applied  $V_{DC}$  bias, thus of the electric field. Such approach has already been reported for the study of both AlGaN and MgZnO alloys.<sup>26,31</sup> However, the higher peak temperature reached by the specimen following laser pulse absorption may activate surface migration phenomena. As a consequence, a reduction of lateral resolution in atom probe 3D reconstructions is observed.<sup>52</sup> A further increase of  $E_{las}$  can even activate long-range surface diffusion phenomena leading to a non-uniform detection of ions over the whole detector. These considerations actually reduce the range of  $E_{las}$ , which is effective for performing La-APT for the given material.

As a final remark, we notice that previous works<sup>20,24</sup> have stated that the measurement of the In III-site fraction by APT is reliable for different crystal orientation of the specimen.

The apparent discrepancy between past results and the present work may be related to the difference in the applied experimental conditions, as well as in the fact that we investigated here the polar orientation, which particularly enhances the effect of field inhomogeneity on the evaporation behavior. In any case, this work points out the primary importance of a careful determination of the experimental conditions where the measurement of an accurate composition at the nanometer scale in InGaN alloys is targeted.

### CONCLUSIONS

The composition of layers of a  $\text{GaN}/\text{Al}_x\text{Ga}_{1-x}\text{N}/\text{In}_y\text{Ga}_{1-y}\text{N}$  LED has been studied by electron microscopy and laser-assisted atom probe tomography. High-resolution dark-field electron

holography allows mapping the projected strain with a subnanometer spatial resolution and assessing the two-dimensional distribution of III-site fraction of  $\text{In}_y\text{Ga}_{1-y}\text{N}$  and  $\text{Al}_x\text{Ga}_{1-x}\text{N}$  layers. Contrarily, 3D atom probe measurements are affected by important compositional biases. The obtained experimental results have shown that the Ga charge-state ratio is a reliable metric for the estimation of the surface electric field during APT analysis. The surface electric field appears to be the main quantity responsible for the inaccuracies of compositional measurements observed for both studied alloys. In particular, we record an increasing deficit of Ga in the composition of both  $\text{Al}_x\text{Ga}_{1-x}\text{N}$  and  $\text{In}_y\text{Ga}_{1-y}\text{N}$  when the surface field is progressively increased. This fact was interpreted in terms of preferential evaporation of Ga atoms between laser pulses due to the applied DC electric field. The origin of such Ga loss cannot be interpreted based on the bulk cohesive energy of the alloy. Indeed, this could be the consequence of the formation of a metallic layer of Ga at the tip surface under N-poor conditions. As Ga-Ga bonds are expected to have a lower binding energy than similar metallic bonds involving In and Al, a large fraction of Ga could evaporate uncorrelated with laser pulses, which can explain the observed loss of detected Ga. These results not only identify a set of experimental conditions for which the accuracy of compositional measurements by APT in III-N ternary alloys is maximized, but also represent a significant gain in the understanding of the complex physics and chemistry of field ion evaporation of these materials.

## SUPPLEMENTARY MATERIAL

See the [supplementary material](#) for the description of the microscopic composition distribution detected for a [0001]-oriented InN specimen.

## ACKNOWLEDGMENTS

This work was funded by the French National Research Agency (ANR) in the framework of the projects EMC3 Labex AQURATE and ANR-13-JS10-0001-01 TAPOTER, by the European Union FP7, NEWLED project (Grant No. 318388), and by the French National Research Agency under the “Investissement d’Avenir” program (Reference No. ANR-10-EQPX-38-01). CEMES acknowledges the “Conseil Regional Midi-Pyrénées” and the European FEDER for financial support within the CPER program. GPM and CEMES acknowledge funding from the METSA Network under Project No. METSA15-B28.

## REFERENCES

- <sup>1</sup>S. Nakamura, M. Senoh, N. Iwasa, and S. I. Nagahama, *Jpn. J. Appl. Phys.* **34**(7A), L797 (1995).
- <sup>2</sup>M. Yamada, Y. Narukawa, and T. Mukai, *Jpn. J. Appl. Phys.* **41**(3A), L246 (2002).
- <sup>3</sup>D. M. Graham, P. Dawson, G. R. Chabrol, and N. P. Hylton, *J. Appl. Phys.* **101**, 033516 (2007).
- <sup>4</sup>D. M. Graham, A. Soltani-Vala, P. Dawson, and M. J. Godfrey, *J. Appl. Phys.* **97**, 103508 (2005).
- <sup>5</sup>D. M. Graham, A. Soltani Vala, P. Dawson, M. J. Godfrey, M. J. Kappers, T. M. Smeeton, J. S. Barnard, C. J. Humphreys, and E. J. Thrush, *Phys. Status Solidi B* **240**(2), 344 (2003).

- <sup>6</sup>S. Kalliakos, P. Lefebvre, X. B. Zhang, T. Taliercio, B. Gil, N. Grandjean, B. Damilano, and J. Massies, *Phys. Status Solidi A* **190**(1), 149 (2002).
- <sup>7</sup>B. Monemar and G. Pozina, *Prog. Quant. Electron.* **24**, 239 (2000).
- <sup>8</sup>S. Grzanka, G. Franssen, G. Targowski, K. Krowicki, T. Suski, R. Czernecki, P. Perlin, and M. Leszczyński, *Appl. Phys. Lett.* **90**, 103507 (2007).
- <sup>9</sup>C. S. Xia, Z. M. Simon Li, and Y. Sheng, *Appl. Phys. Lett.* **103**, 233505 (2013).
- <sup>10</sup>T. M. Smeeton, M. J. Kappers, J. S. Barnard, M. E. Vickers, and C. J. Humphreys, *Appl. Phys. Lett.* **83**(26), 5419 (2003).
- <sup>11</sup>A. Rosenauer, T. Mehrrens, K. Muller, K. Gries, M. Schowalter, P. Venkata Satyam, S. Bley, C. Tessarek, D. Hommel, K. Sebald, M. Seyfried, J. Gutowski, A. Avramescu, K. Engl, and S. Lutgen, *Ultramicroscopy* **111**, 1316 (2011).
- <sup>12</sup>M. J. Galtrey, R. A. Oliver, M. J. Kappers, and C. J. Humphreys, *Appl. Phys. Lett.* **90**, 061903 (2007).
- <sup>13</sup>M. J. Galtrey, R. A. Oliver, M. J. Kappers, C. McAleese, D. Zhu, C. J. Humphreys, P. H. Clifton, D. Larson, and A. Cerezo, *Appl. Phys. Lett.* **92**(4), 041904 (2008).
- <sup>14</sup>F. Liu, L. Huang, R. F. Davis, L. M. Porter, D. K. Schreiber, S. V. Kuchibatla, V. Shutthanandan, S. Thevuthasan, E. A. Preble, T. Paskova, and K. R. Evans, *J. Vac. Sci. Technol. B* **32**(5), 051209 (2014).
- <sup>15</sup>J. T. Griffiths, F. Oehler, F. Tang, S. Zhang, W. Yuen Fu, T. Zhu, S. D. Findlay, C. Zheng, J. Etheridge, T. L. Martin, P. A. J. Bagot, M. P. Moody, D. Sutherland, P. Dawson, M. J. Kappers, C. J. Humphreys, and R. A. Oliver, *J. Appl. Phys.* **119**, 175703 (2016).
- <sup>16</sup>T. Mehrrens, M. Schowalter, D. Tytko, P. Choi, D. Raabe, L. Hoffmann, H. Jönen, U. Rossow, A. Hangleiter, and A. Rosenauer, *Appl. Phys. Lett.* **102**, 132112 (2013).
- <sup>17</sup>B. Bonef, M. Catalano, C. Lund, S. P. DenBaars, S. Nakamura, U. K. Mishra, M. J. Kim, and S. Keller, *Appl. Phys. Lett.* **110**, 143101 (2017).
- <sup>18</sup>T. J. Prosa, P. H. Clifton, H. Zhong, A. Tyagi, R. Shivaraman, S. P. DenBaars, S. Nakamura, and J. S. Speck, *Appl. Phys. Lett.* **98**, 191903 (2011).
- <sup>19</sup>D. J. Larson, T. J. Prosa, D. Olson, W. Lefebvre, D. Lawrence, P. H. Clifton, and T. F. Kelly, *J. Phys. Conf. Ser.* **471**, 012030 (2013).
- <sup>20</sup>L. Mancini, D. Hernández-Maldonado, W. Lefebvre, J. Houard, I. Blum, F. Vurpillot, J. Eymery, C. Durand, M. Tchernycheva, and L. Rigutti, *Appl. Phys. Lett.* **108**, 042102 (2016).
- <sup>21</sup>J. R. Riley, S. Padalkar, Q. Li, P. Lu, D. D. Koleske, J. J. Wierer, G. T. Wang, and L. J. Lauhon, *Nano Lett.* **13**(9), 4317 (2013).
- <sup>22</sup>M. Khoury, H. Li, B. Bonef, L. Y. Kuritzky, A. J. Mughal, S. Nakamura, J. S. Speck, and S. P. DenBaars, *Appl. Phys. Express* **11**, 036501 (2018).
- <sup>23</sup>H. Li, M. Khoury, B. Bonef, A. I. Alhassan, A. J. Mughal, E. Azimah, M. E. A. Samsudin, P. De Mierry, S. Nakamura, J. S. Speck, and S. P. DenBaars, *ACS Appl. Mater. Interfaces* **9**(41), 36417 (2017).
- <sup>24</sup>J. R. Riley, T. Detchprohm, C. Wetzel, and L. J. Lauhon, *Appl. Phys. Lett.* **104**, 152102 (2014).
- <sup>25</sup>L. Mancini, N. Amirifar, D. Shinde, I. Blum, M. Gilbert, A. Vella, F. Vurpillot, W. Lefebvre, R. Lardé, E. Talbot, P. Pareige, X. Portier, A. Ziani, C. Davesne, C. Durand, J. Eymery, R. Butté, J.-F. Carlin, N. Grandjean, and L. Rigutti, *J. Phys. Chem. C* **118**, 24136 (2014).
- <sup>26</sup>E. Di Russo, F. Moyon, N. Gogneau, L. Largeau, E. Giraud, J.-F. Carlin, N. Grandjean, J. Michel Chauveau, M. Hugues, I. Blum, W. Lefebvre, F. Vurpillot, D. Blavette, and L. Rigutti, *J. Phys. Chem. C* **122**(29), 16704 (2018).
- <sup>27</sup>E. Di Russo, I. Blum, J. Houard, M. Gilbert, G. Da Costa, D. Blavette, and L. Rigutti, *Ultramicroscopy* **187**, 126 (2018).
- <sup>28</sup>E. Di Russo, I. Blum, J. Houard, G. Da Costa, D. Blavette, and L. Rigutti, *Microsc. Microanal.* **23**(6), 1067 (2017).
- <sup>29</sup>B. Bonef, R. Cramer, and J. S. Speck, *J. Appl. Phys.* **121**, 225701 (2017).
- <sup>30</sup>L. Rigutti, L. Mancini, D. Hernández-Maldonado, W. Lefebvre, E. Giraud, R. Butté, J. F. Carlin, N. Grandjean, D. Blavette, and F. Vurpillot, *J. Appl. Phys.* **119**, 105704 (2016).
- <sup>31</sup>E. Di Russo, “Study of the physical mechanisms leading to compositional biases in atom probe tomography of semiconductors,” Ph.D. thesis, Normandie Université, 2018.

- <sup>32</sup>R. J. H. Morris, R. Cuduvally, D. Melkonyan, C. Fleischmann, M. Zhao, L. Arnoldi, P. van der Heide, and W. Vandervorst, *J. Vac. Sci. Technol. B* **36**(3), 03F130 (2018).
- <sup>33</sup>B. Gault, D. W. Saxey, M. V. Ashton, S. B. Sinnott, A. N. Chiaromonti, M. P. Moody, and D. K. Schreiber, *New J. Phys.* **18**, 033031 (2016).
- <sup>34</sup>D. R. Diercks, B. P. Gorman, R. Kirchhofer, N. Sanford, K. Bertness, and M. Brubaker, *J. Appl. Phys.* **114**, 184903 (2013).
- <sup>35</sup>A. F. Tsatsulnikov, W. V. Lundin, A. V. Sakharov, A. E. Nikolaev, E. E. Zavarin, S. O. Usov, M. A. Yagovkina, M. J. Hÿtch, M. Korytov, and N. Cherkashin, *Sci. Adv. Mater.* **7**(8), 1629 (2015).
- <sup>36</sup>S. Padalkar, J. R. Riley, Q. Li, G. T. Wang, and L. J. Lauhon, *Phys. Status Solidi C* **11**(3–4), 656 (2014).
- <sup>37</sup>I. Blum, F. Cuvilly, and W. Lefebvre-Ulrikson, “Atom probe sample preparation,” in *Atom Probe Tomography* (Academic Press, 2016).
- <sup>38</sup>J. Bogdanowicz, A. Kumar, C. Fleischmann, M. Gilbert, J. Houard, A. Vella, and W. Vandervorst, *Ultramicroscopy* **188**, 19 (2018).
- <sup>39</sup>M. J. Hÿtch, F. Houdellier, F. Hÿe, and E. Snoeck, *J. Phys. Conf. Ser.* **241**, 012027 (2010).
- <sup>40</sup>N. Cherkashin, S. Reboh, A. Lubk, M. J. Hÿtch, and A. Claverie, *Appl. Phys. Express* **6**, 091301 (2013).
- <sup>41</sup>K. Pantzas, G. Patriarche, D. Troadec, M. Kociak, N. Cherkashin, M. Hÿtch, J. Barjon, C. Tanguy, T. Rivera, S. Suresh, and A. Ougazzaden, *J. Appl. Phys.* **117**, 055705 (2015).
- <sup>42</sup>N. N. Ledentsov, V. A. Shchukin, Y. M. Shernyakov, M. M. Kulagina, A. S. Payusov, N. Y. Gordeev, M. V. Maximov, A. E. Zhukov, T. Denneulin, and N. Cherkashin, *Opt. Express* **26**(11), 13985 (2018).
- <sup>43</sup>M. J. Hÿtch, C. Gatel, and K. Ishizuka, *HoloDark Phase* (HREM Research, 2010).
- <sup>44</sup>N. Cherkashin, M. J. Hÿtch, E. Snoeck, F. Hÿe, J. M. Hartmann, Y. Bogumilowicz, and A. Claverie, *Nucl. Instrum. Methods Phys. Res. B* **253**(1–2), 145 (2006).
- <sup>45</sup>N. Cherkashin, M. J. Hÿtch, F. Houdellier, F. Hÿe, V. Paillard, A. Claverie, A. Gouy e, O. Kermarrec, D. Rouchon, M. Burdin, and P. Holliger, *Appl. Phys. Lett.* **94**(14), 141910 (2009).
- <sup>46</sup>N. Cherkashin, S. Reboh, M. J. Hÿtch, A. Claverie, V. V. Preobrazhenskii, M. A. Putyato, B. R. Semyagin, and V. V. Chaldyshev, *Appl. Phys. Lett.* **102**, 173115 (2013).
- <sup>47</sup>G. Da Costa, F. Vurpillot, A. Bostel, and B. Deconihout, *Rev. Sci. Instrum.* **76**, 013304 (2005).
- <sup>48</sup>G. Da Costa, H. Wang, S. Duguay, A. Bostel, D. Blavette, and B. Deconihout, *Rev. Sci. Instrum.* **83**, 123709 (2012).
- <sup>49</sup>P. Li, B. Bonef, M. Khoury, G. Lheureux, H. Li, J. Kang, S. Nakamura, and S. P. DenBaars, *Superlattices Microstruct.* **113**, 684 (2018).
- <sup>50</sup>D. R. Kingham, *Surf. Sci.* **116**, 273 (1982).
- <sup>51</sup>M. M uller, D. W. Saxey, G. D. W. Smith, and B. Gault, *Ultramicroscopy* **111**, 487 (2011).
- <sup>52</sup>B. Gault, M. M uller, A. La Fontaine, M. P. Moody, A. Shariq, A. Cerezo, S. P. Ringer, and G. D. W. Smith, *J. Appl. Phys.* **108**, 044904 (2010).
- <sup>53</sup>D. Zanuttini, I. Blum, E. Di Russo, L. Rigutti, F. Vurpillot, J. Douady, E. Jacquet, P.-M. Anglade, and B. Gervais, *J. Chem. Phys.* **149**, 134311 (2018).
- <sup>54</sup>A. Costales, M. A. Blanco,  . Mart ın Pend as, A. K. Kandalam, and R. Pandey, *J. Am. Chem. Soc.* **124**(15), 4116 (2002).
- <sup>55</sup>C. Stampfl and C. G. Van der Walle, *Phys. Rev. B* **59**, 5521 (1999).
- <sup>56</sup>J. Neugebauer, T. Zywietz, M. Scheffler, and J. Northrup, *Appl. Surf. Sci.* **159–160**, 355 (2000).
- <sup>57</sup>E. Di Russo, J. Houard, V. Langolf, S. Moldovan, L. Rigutti, B. Deconihout, D. Blavette, J. Bogdanowicz, and A. Vella, *Appl. Phys. Lett.* **112**, 143103 (2018).
- <sup>58</sup>J. Nord, K. Albe, P. Erhart, and K. Nordlund, *J. Phys. Condens. Matter* **15**(32), 5649 (2003).
- <sup>59</sup>J. E. Northrup, J. Neugebauer, R. M. Feenstra, and A. R. Smith, *Phys. Rev. B* **61**(15), 9932 (2000).
- <sup>60</sup>C. Adelman, J. Brault, G. Mula, B. Daudin, L. Lymparakis, and J. Neugebauer, *Phys. Rev. B* **67**(16), 165419 (2003).
- <sup>61</sup>E. P. Silaeva, L. Arnoldi, M. L. Karahka, B. Deconihout, A. Menand, H. J. Kreuzer, and A. Vella, *Nano Lett.* **14**(11), 6066 (2014).